UC Santa Cruz
UC Santa Cruz Previously Published Works

Title

Geometry of Pentaphenylantimony in Solution: Support for a Trigonal Bipyramidal Assignment from X-ray Absorption Spectroscopy and Vibrational Spectroscopic Data

Permalink

Journal

ISSN

Authors

Lindquist-Kleissler, Brent
Weng, Monica
Le Magueres, Pierre
et al.

Publication Date

DOI

Peer reviewed

Analysis of Oxygen–Pnictogen Bonding with Full Bond Path Topological Analysis of the Electron Density

Brent Lindquist-Kleissler, John S. Wenger, and Timothy C. Johnstone*

Department of Chemistry and Biochemistry, University of California, Santa Cruz, Santa Cruz, California 95064, United States.

ABSTRACT A variety of methods are available to investigate the bonding in inorganic compounds. In contrast to wavefunction-based analyses, topological analysis of the electron density affords the advantage of analyzing a physical observable: the electron density. Classical topological analyses of bonding interactions within the Atoms in Molecules framework typically involve location of a bond path between two atoms and evaluation of a range of real-space functions at the $(3, -1)$ critical point in the electron density that exists on that bond path. We show here that counter-intuitive trends are obtained from the analysis of the electron density (ρ), the Laplacian ($\nabla^2\rho$), and ellipticity (ε) at the O–E $(3, -1)$ critical points in the CCSD electron densities of a series of compounds featuring a range of oxygen–pnictogen bond types: EO^+, HEO, H_2EOH, H_3EOH^+ and H_3EO (where E = N, P, As, Sb, or Bi). If, instead, these real-space functions are evaluated along the length of the bond path, the discrepancies in the trends are resolved. We show that robust results are also obtained using electron densities from less computationally demanding DFT calculations. The increased computational efficiency allowed us to also investigate organic derivatives of these oxygen–pnictogen bonded compounds and observe that the trends hold in these instances as well. We anticipate that these results will be of use to inorganic chemists engaged in the synthesis and evaluation of novel bonding interactions, particularly those involving heavy main-group elements.

INTRODUCTION

The chemistry of the group 15 elements, or pnictogens, varies greatly down the family from non-metallic N and P, through metalloid As and Sb, to metallic Bi.[1] The unique chemistry of the pnictogens has permitted innovations ranging from new catalysts and sensors to new paradigms for interpreting chemical structure and reactivity.[2-5] Central to these advances is the characteristic nature of the bonding interactions in which pnictogens engage. In both theoretical and experimental approaches, homologous series of pnictogen-containing compounds have allowed fundamental concepts of structure and bonding to be tested and have revealed systematic variation across the periods. Such systematic variation is readily observed in the fluxionality of EH_5 species,[6] the interatomic angles of EH_3 compounds,[7] secondary (pnictogen) bonding capacity,[8] the structure and electronic properties of OCE^- anions,[9] and the multiple bonding in dipnictenes,[10] to name a few. These variations have informed our understanding of the roles of hybridization, relativity, and orbital overlap in main-group chemistry.[1]

The interactions of the pnictogens with oxygen are richly varied and of great importance. The pnictogen elements all readily combine with oxygen. On a terrestrial scale, the oxides of nitrogen play an important role in atmospheric chemistry and the oxides of the heavier pnictogens play an important role in geochemistry.[11] Biologically, oxygen–phosphorus bonds are central to manifold processes, including bioenergetics (ATP/ADP), genetic information storage (DNA/RNA phosphodiesters), and cell function (protein phosphorylation).[12] Arsenic oxides feature in the mechanism of action of anticancer and antiparasitic dugs.[13] Compounds with oxygen–antimony bonds are widely used as flame retardants but also find applications as antiparasitic drugs.[14] Bismuth oxides have been used in fireworks and dental fixtures, and

compounds containing oxygen–bismuth bonds have been implicated in the biological activity of bismuth subsalicylate (Pepto-Bismol[TM]).[15]

Molecular species featuring O–E bonds exhibit a rich diversity of interactions ranging from the formal triple bonds of EO^+ diatomic cations isoelectronic with N_2 to the O–E single bonds in species like hydroxylamine (H_2NOH) or phosphinous acid (H_2POH). The nature of the O–E bonding in R_3EO compounds, which include such commonly encountered species as trimethylamine *N*-oxide and triphenylphosphine oxide, has long served as a point of discussion.[16-24] The amine oxides are conventionally depicted with a polar single bond ($O^-–N^+$) but the heavier congeners are conventionally shown with a double bond (O=E). It is now well established, however, that the d orbitals of these heavier pnictogens do not participate in bonding.[1] Nevertheless, the O–E interaction in these R_3EO species is quite distinct from that of other EO functional groups, as reflected in their distinct reactivity.[25]

The structures and reactivities of these different classes of oxygen–pnictogen compounds have been analyzed and rationalized through a host of different electronic structure analytical frameworks. Among the most common are methods that involve analysis of the canonical molecular orbitals (MOs) obtained from diagonalization of the Fock matrix. Alternative MO schemes, obtained by applying unitary transformations to the canonical MOs, have also been used to analyze oxygen–pnictogen bonding. One prominent example is natural bond orbital (NBO) analysis.[26] The molecular orbitals used to investigate chemical bonding, whether canonical or transformed, are typically obtained using the Hartree-Fock (HF) self-consistent field theory and can be modified to account for the influence of electron-electron correlation according to a variety of post-HF schemes (e.g., Møller–Plesset perturbation theory, configuration interaction, coupled-cluster theory, etc.). Alternatively, the Kohn-Sham orbitals

obtained from density functional theory (DFT) calculations can be analyzed directly or following

unitary transformation.[27]

A strategy that complements these orbital-based analyses is the topological analysis of

the electron density, commonly referred to as Atoms in Molecules (AIM) or the Quantum

Theory of Atoms in Molecules (QTAIM).[28,29] One notable difference between analysis of

electron density and analysis of wavefunctions is that the former relies exclusively on a physical

observable. In practice, this electron density is typically obtained from wavefunction or DFT

calculations, but it need not be; refined charge densities from high-resolution X-ray diffraction

allow experimental electron densities to be analyzed. Based on our interest in the medicinal

inorganic chemistry of pnictogen-containing species, we sought a framework through which to

classify and categorize oxygen–pnictogen bonds through a topological analysis of the electron

density. Many different methods can be used to compare and contrast the bonding in these

molecules, but topological analysis of the electron density is unique in that it remains agnostic to

the origin of that electron density. Although isolated studies have been performed on subsets of

oxygen–pnictogen compounds, to the best of our knowledge no systemic investigation of the

topology of electron density of these compounds has been performed.

The details of the topological analysis of electron density (ρ) within the AIM framework

have been extensively covered previously, and we refer the reader to those comprehensive

resources for details.[28,29] We will briefly introduce here those concepts necessary for the ensuing

discussion. Two functions whose topologies are extensively probed are ρ and the Laplacian of

the electron density ($\nabla^2\rho$), the latter of which is equal to the sum of the eigenvalues λ_1, λ_2, and λ_3

of the Hessian of ρ. The Hessian matrix comprises the partial second derivatives of ρ with

respect to orthogonal spatial directions. A key feature of these analyses is the identification of

topologically critical points in ρ or $\nabla^2\rho$. Critical points in ρ are points in three-dimensional space where the gradient of the electron density ($\nabla\rho$) vanishes. These critical points are classified according to the properties of the Hessian of ρ at this point in space, which are summarized by the rank and signature. The rank (ω) is the number of non-zero curvatures (Hessian eigenvalues) in ρ at the critical point and the signature (σ) is the algebraic sum of the signs of the curvatures (Hessian eigenvalues) at the critical point. The vector field $\nabla\rho$ also features prominently in the theory of Atoms in Molecules. It comprises field lines that either (i) originate at infinity and terminate at a critical point or (ii) link two critical points. One of the most fascinating features of the topology of ρ is that the critical points and the gradient paths that link them recover our conventional notions of molecular structure.[30] Nuclear positions are reflected by critical points in ρ with $\omega = 3$ and $\sigma = -3$, also known as $(3, -3)_\rho$ critical points. A $(3, -1)_\rho$ critical point will lie between any two atoms engaged in a bonding interaction and two unique gradient paths will link this $(3, -1)_\rho$ critical point to the two $(3, -3)_\rho$ critical points associated with the bonded atoms. Combined, these two gradient trajectories form a *bond path* and the union of all the $(3, -3)_\rho$ critical points and bond paths comprises the molecular graph.

The fidelity with which known bonding interactions have mapped onto $(3, -1)_\rho$ critical points has led many investigators to use the presence of such a critical point as evidence of a bonding interaction,[30] although dogmatic reliance on this correspondence has been questioned.[31] In addition to providing evidence of a bonding interaction, topological analyses can also shed light on the nature of the bond.[32] A rich array of analyses can be performed to provide nuanced information on bonding, but most investigations follow a typical formula. First, ρ is searched to locate a $(3, -1)_\rho$ critical point linked to two $(3, -3)_\rho$ critical points via unique $\nabla\rho$ trajectories. The values of a variety of real-space functions are then evaluated at the $(3, -1)_\rho$ critical point.

Although the list of real-space functions employed in this capacity continues to grow, among the most widely used and robust are: ρ itself, $\nabla^2\rho$, and the ellipticity ($\varepsilon = \lambda_1/\lambda_2 - 1$). The value of ρ at the $(3, -1)_\rho$ critical point tends to track with the strength of the bond and the bond order. The Laplacian reflects local concentrations and depletions in ρ. Negative values of $\nabla^2\rho$ at the $(3, -1)_\rho$ critical point are generally observed for covalent interactions; stronger or higher-order covalent bonds generally feature more negative values of $\nabla^2\rho$. Conversely, closed-shell interactions (e.g., ionic or dative bonding) typically feature positive values of $\nabla^2\rho$ at the $(3, -1)_\rho$ critical point. Finally, ε provides a measure of the extent to which ρ is preferentially accumulated in the plane defined by the eigenvectors of the Hessian associated with λ_1 and λ_3.[33,34] Note that, at the $(3, -1)_\rho$ critical point, λ_1 is the negative curvature of greatest magnitude and λ_3 is the positive curvature in the direction of the bond path. For bonds with cylindrical σ symmetry, $\varepsilon = 0$, whereas for those with elliptical π symmetry, $\varepsilon > 0$.

It is important to note, however, that many of the relationships identified between the nature of a bond and values of ρ, $\nabla^2\rho$, and ε at $(3, -1)_\rho$ critical points of covalent bonds were established using relatively non-polar bonds between first- and second-period elements. Studies of polar covalent bonds and bonds involving heavier elements have shown that reliance on the values of these functions at the $(3, -1)_\rho$ critical point alone can be misleading.[35-42] As described below, our initial investigation of oxygen–pnictogen bonding revealed that the values of ρ, $\nabla^2\rho$, and ε at the $(3, -1)_\rho$ critical points of a variety of O–E bonds did not trend as expected. We found, however, that analysis of these functions *along the length of the bond path* recovers the expected trends across the pnictogen family. In addition to providing insight into the bonding in these molecules, this bond path topological analysis also reveals patterns that are characteristic of each of the bond types explored herein (O–E, O=E, O≡E, $O^-–E^+$). We show that the same

patterns are produced regardless of whether ρ is obtained from coupled-cluster (CCSD) or DFT calculations. The patterns also persist upon substitution with organic groups.

RESULTS AND DISCUSSION

Classical examples/references. The trends that have been established between bond types and the values of different real-space functions at $(3, -1)_\rho$ critical points were initially observed in relatively non-polar bonds between light atoms. Consider the members of the series comprising ethane, ethene, and ethyne, which all feature a $(3, -1)_\rho$ critical point between the two carbon atoms. A depiction of ρ along the bond path readily reveals the local minimum coincident with the critical point, which lies exactly halfway between the two carbon atoms for each molecule (Figure 1A). Note that, in Figure 1, the bond distances were normalized to unit length to facilitate the comparison of species with different bond lengths. The value of ρ at the $(3, -1)_\rho$ critical point (ρ_b) tracks with bond order and steadily increases from single to double to triple bond. For all three of these molecules, the value of $\nabla^2\rho$ at the $(3, -1)_\rho$ critical point ($\nabla^2\rho_b$) is negative, as expected for a covalent bond in which electron density is locally concentrated between the nuclei (Figure 1B). Additionally, $\nabla^2\rho_b$ becomes increasingly negative from single to double to triple bond. Finally, the ellipticity at the $(3, -1)_\rho$ critical point (ε_b) is zero for the cylindrically symmetric single and triple bonds of ethane and ethyne, but non-zero for ethene because of the preferential concentration of electron density above and below the plane of the molecule (Figure 1C).
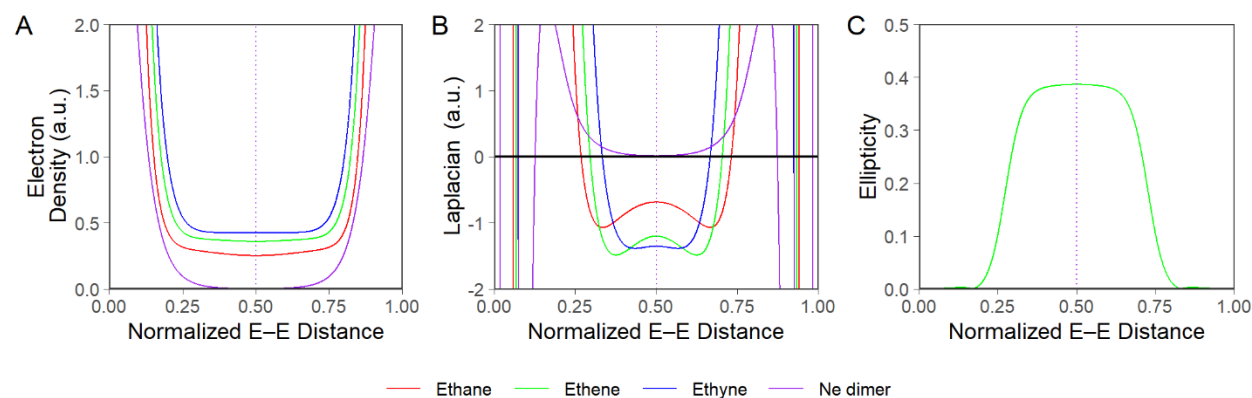
Figure 1. Plots of (A) ρ, (B) $\nabla^2\rho$, and (C) ε as a function of the normalized C–C (for ethane, ethene, and ethyne) or Ne–Ne (for Ne dimer) bond length for a series of reference compounds. For (C), note that ethane, ethyne, and Ne_2 have $\varepsilon = 0$ along the length of the bond. Orbital-optimized electron densities were obtained from single-point CCSD/ANO-RCC-QZP calculations at experimental geometries extracted from the NIST CCCDB.[43] See Figure S2 for CVD balanced image.

The covalent bonding in the ethane/ethene/ethyne series is fundamentally different in nature from the bonding that is present in the van der Waals molecule Ne_2.[44] This latter compound still features a $(3, -1)_\rho$ critical point between the two nuclei, but the value of ρ_b is exceedingly small, reflecting the weak strength of the bond. The value of $\nabla^2\rho_b$ is negligibly small and positive, consistent with the non-covalent nature of the interaction. As expected, $\varepsilon_b = 0$ for the cylindrically symmetric Ne_2. The values of these functions at the $(3, -1)_\rho$ critical points are summarized in Table 1.

Table 1. Values of Real-Space Functions at $(3, -1)_\rho$ Critical Points of Reference Compounds [a]

	ρ_b (a.u.)	$\nabla^2\rho_b$ (a.u.)	ε_b
Ethane	0.252	-0.686	0.000

Ethene	0.359	-1.202	0.387
Ethyne	0.425	-1.354	0.000
Ne dimer	0.002	0.013	0.000

[a] Electron densities obtained from orbital-optimized single-point CCSD/ANO-RCC-QZP calculations.

Panel selection. Our initial goal was to establish the periodic trends that exist in oxygen–pnictogen bonds across group 15 and across the accessible bond orders. Oxygen can readily form nominal triple, double, and single bonds with the pnictogens. We selected five classes of compounds: EO^+, HEO, H_2EOH, H_3EOH^+, and H_3EO (Chart 1). The EO^+ cations are formally isoelectronic with N_2 and feature a triple bond. The HEO species exhibit the canonical oxygen–pnictogen double bond. The H_2EOH species feature an oxygen–pnictogen single bond. To establish whether the valence of the pnictogen influences our results, the pentavalent H_3EOH^+ species, which also contain formal O–E single bonds, were investigated. The final class of compounds comprised the pentavalent H_3EO species. These compounds could naively be considered as the pentavalent analogues of the HEO compounds given that they are often written as having double bonds (e.g. $Ph_3P=O$), but it is now well accepted that the EO bonds in these compounds are distinct from either conventional single or double bonds.[18]

Chart 1. Structures of the Classes of Compounds Investigated
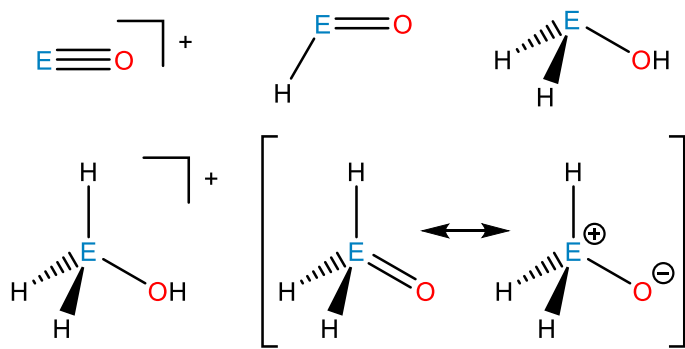
The geometries of the molecules were optimized at the MP2/def2-QZVPP level of theory, which provides structures that agree with those that have been experimentally determined by spectroscopic or diffractometric methods (Table S1). We note that the def2-QZVPP basis set[45] used in the geometry optimizations employs effective core potentials to address relativistic effects, which become particularly important for the antimony and bismuth compounds. The final electron densities were obtained at the MP2-optimized geometries from orbital-optimized CCSD/ANO-RCC-QZP single-point energy calculations. In these calculations, the second-order Douglas-Kroll-Hess method was used in conjunction with a relativistically contracted, correlation-consistent, all-electron, quadruple-ζ atomic natural orbital basis set to account for relativistic effects.[46,47]

Critical point analyses of oxygen–pnictogen compounds. Analysis of ρ for the 15 compounds in Chart 1 identified a clear $(3, -1)_\rho$ critical point between the oxygen and pnictogen atoms. In the vein of conventional analyses, ρ_b, $\nabla^2\rho_b$, and ε_b were evaluated at each $(3, -1)_\rho$ critical point (Figure 2; Table S2). Among the E = N species, ρ_b decreases steadily from triply-bonded NO^+ to doubly-bonded HNO to singly-bonded H_2NOH and H_3NOH^+(Figure 2A). The two singly-bonded species exhibit relatively similar values of ρ_b, with that of H_3NOH^+ being slightly higher. The value of ρ_b for H_3NO lies between that of the doubly- and singly-bonded species, albeit more closely to the single-bond values. The same trend is broadly observed when E = P, As, Sb, or Bi, although the range of values is much narrower. The EO^+ species consistently exhibit a ρ_b value higher than that of HEO, which is in turn higher than those of H_2EOH and H_3EOH^+. Among the singly-bonded species, ρ_b is consistently greater for H_3EOH^+. One significant difference from the N compounds is that the heavier H_3EO species all feature ρ_b values greater than those of the doubly-bonded HEO species. The ρ_b value for H_3EO

progressively approaches the value for EO$^+$ as the family is descended. Comparing across the family within each class of compounds, we observe a systematic decrease in ρ_b with increasing atomic number, consistent with the expected decrease in orbital overlap in the bonds involving the large, heavy atoms. The dramatic change from N to P followed by more subtle variation further down the family is consistent with the generally observed principle that bonding between second-period elements differs greatly from that of the heavier elements, which are generally more similar. Nonetheless, there is a consistent trend across the whole family. Similar trends exist among the atomic charges obtained by integrating electron density within the topologically defined atomic basins (Table S3). Note that, unlike the heavier pnictogens, nitrogen is more electronegative than H, so for all classes of compounds with E–H bonds, the nitrogen members have negative charges. Among the heavier elements, the O–P charge separation is consistently greatest and those of the remaining species differ little. There is also little variation across bond types, with the exception that all charge separations are greater for the E(V) species, as expected.
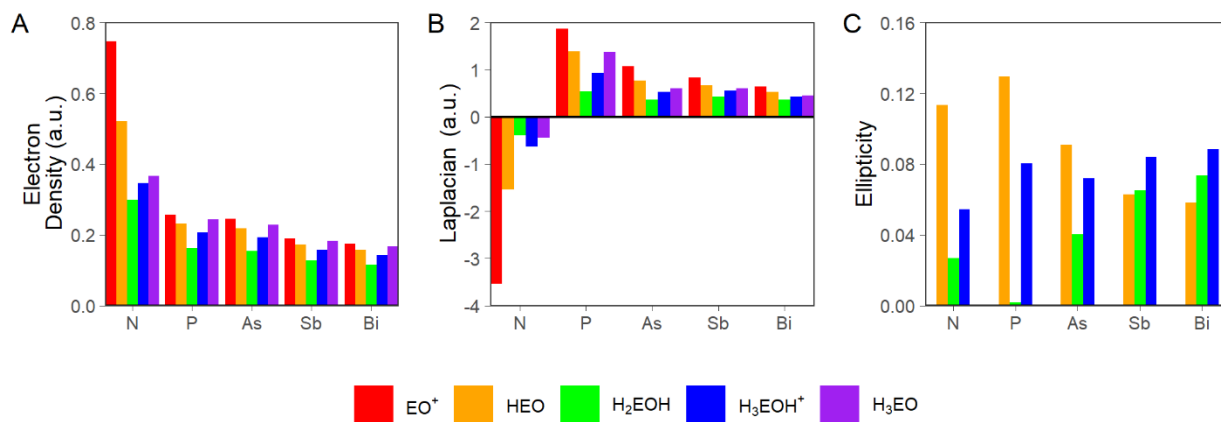

Figure 2. Values of (A) ρ_b, (B) $\nabla^2\rho_b$, and (C) ε_b for all 15 species grouped by pnictogen and colored by compound type. For (C), note that all EO$^+$ and H$_3$EO compounds have ε_b = 0. Note that ρ_b,

$\nabla^2\rho_b$, and ε_b are the values of ρ, $\nabla^2\rho$, and ε at the (3,–1) critical point in ρ. See Figure S3 for CVD balanced image.

A similarly consistent trend is not found among the values of $\nabla^2\rho_b$ (Figure 2B). Among the E = N species, the $\nabla^2\rho_b$ values trend as expected. All compounds have $\nabla^2\rho_b < 0$, consistent with a covalent interaction between the N and O atoms. For the triply-bonded NO^+, $\nabla^2\rho_b$ is the most negative, followed by HNO, and then H_3NOH^+ and H_2NOH. The $\nabla^2\rho_b$ value for H_3NO lies between the values for the two singly-bonded species. These values vary with bond order in the same way as those of ethane, ethene, and ethyne (Table 1). For all compounds of the heavier elements, however, $\nabla^2\rho_b > 0$. The pattern among the phosphorus compounds is nearly the mirror image of that for the nitrogen compounds. PO^+ has the most positive value of $\nabla^2\rho_b$, followed by HPO and then H_3POH^+ and H_2POH. H_3PO has a value of $\nabla^2\rho_b$ between that of the singly- and doubly-bonded compounds. This trend of positive $\nabla^2\rho_b$ values is displayed by all of the heavier pnictogen series, with the absolute values of the Laplacian gradually decreasing down the family. The value of $\nabla^2\rho_b$ is often taken as a strong indicator of the nature of the bond, with negative values suggesting an open-shell, or covalent, interaction and positive values suggesting a closed-shell interaction. As with ρ_b, the $\nabla^2\rho_b$ values highlight the distinction between the bonding in oxygen–nitrogen compounds and that in all of the other oxygen–pnictogen compounds. But in contrast to ρ_b, which only signified a difference in the magnitude of the interaction, $\nabla^2\rho_b$ appears to suggest a fundamentally different kind of interaction. The data could be interpreted as suggesting that the formally triply-bonded PO^+ does not have a covalent bond. As with ρ_b, the spread of $\nabla^2\rho_b$ values across the different bond types decreases dramatically down the family.

In an effort to gain further insight into the variation in bonding across these series, and to find metrics that provide greater discriminatory power for the O–E bonds of the heavier pnictogens, we determined the values of ε_b (Figure 2C). Among the nitrogen-containing molecules, ε_b takes on the expected value of 0 for the cylindrically symmetric NO^+. For the doubly-bonded, π-symmetric HNO, ε_b takes on a positive value, albeit one lower than that of the C=C bond in ethene (Table 1). For the singly-bonded H_2NOH and H_3NOH^+, ε_b does not assume the expected value of 0 (cf. ethane, Table 1) but the magnitude is nonetheless less than that of HNO. As was the case for ρ_b and $\nabla^2\rho_b$, the magnitude of ε_b of H_3NOH^+ is slightly greater than that of H_2NOH. Finally, for the cylindrically symmetric H_3NO, $\varepsilon_b = 0$ as expected. For the heavier pnictogens (E = P, As, Sb, or Bi), $\varepsilon_b = 0$ for the cylindrically symmetric EO^+ and H_3EO species, as expected. Moreover, the HEO compounds feature positive ε_b values that decrease in magnitude down the family, as would be expected based on the decreased efficiency of multiple bonding as the family is descended. Among the singly-bonded species, however, the ε_b values do not trend as expected. H_2POH features an ε_b of approximately zero, closer to expectation than H_2NOH, but for H_3POH^+ ε_b is over half that of the doubly-bonded HPO. As the pnictogen increases in atomic number, the ε_b values for the singly-bonded species consistently *increase* and for and Sb and Bi they overtake the value of the corresponding HEO compound. An argument can be made for an expected increase in ε_b as the atomic number of E in H_2EOH increased because the E–H σ^* orbital lowers in energy, facilitating a lone pair (O) to σ^* (E–H) transition. It is nevertheless surprising that an increase in ε_b via this mechanism would cause the ε_b values of H_2EOH to overtake those of HEO, with formal O=E double bonds.

Bond path analyses of oxygen–pnictogen compounds. To gain further insight into the anomalous trends observed in the values of the real-space functions evaluated at the $(3, -1)_\rho$

critical points, ρ, $\nabla^2\rho$, and ε were evaluated along the entire length of the O–E bond (Figure 3). To facilitate the comparison of species with differing bond lengths, the O–E distances of all compounds were normalized to unit length. Along each bond path, a clear minimum is observed in ρ, coincident with a $(3, -1)_\rho$ critical point (Figure 3A–E). The difference in electronegativity of the bonded elements imparts polarity on the bond as reflected in the skewed distribution of ρ along the bond path. Among the nitrogen-containing species, as the bond order decreases, the bond lengthens, the electron density distribution trends towards more symmetric, and the $(3, -1)_\rho$ critical point moves toward the midway point of the bond. For the heavier pnictogens, the longer bonds vary less in length across bond orders, and the trend is less pronounced. In all compound classes, as the pnictogen increases in size, the bond length increases and the proportion of the bond attributable to oxygen decreases, which manifests as a gradual migration of the critical point toward the oxygen along the normalized bond. The location of the $(3, -1)_\rho$ critical point is marked with a dashed vertical line in all panels of Figure 3, and the intersection of the dashed line with the solid curve provides the values depicted in Figure 2 and collected in Table S2. As noted above, the values of ρ_b do indeed follow the expected trends, but the full curves depicted in Figure 3 better capture the gradual variation in ρ that occurs across the pnictogen family.
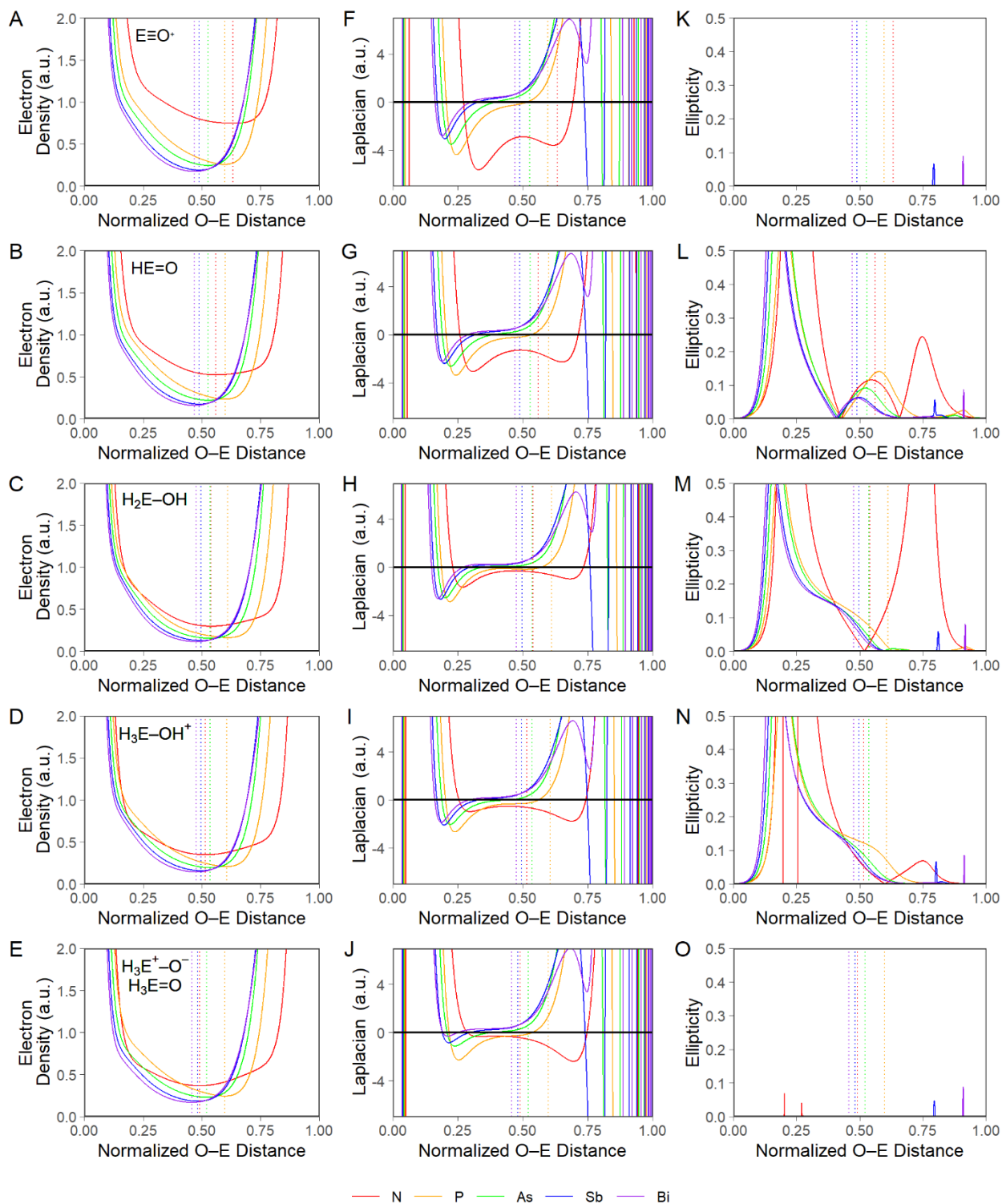
Figure 3. Evaluation (CCSD/ANO-RCC-QZP//MP2/def2-QZVPP) of electron density, Laplacian, and ellipticity along the normalized oxygen–pnictogen bond paths of different compounds (O at

0.0 and E and 1.0). Rows of panels feature data for a class of compounds: EO^+ (A, F, K); HEO (B, G, L); H_2EOH (C, H, M); H_3EOH^+ (D, I, N); and H_3EO (E, J, O) where E is a pnictogen. For (K) and (O), note that all compounds have $\varepsilon = 0$ along the length of the bond. Dashed vertical lines represent the location of the bond critical point. See Figure S4 for CVD balanced image.

Analysis of the plots of $\nabla^2\rho$ for the nitrogen compounds (Figure 3F–J) reveals that they have overall shapes similar to those of the curves for ethane, ethene, and ethyne (Figure 1B). It should be noted that the concentrations of nearly vertical lines near 0 and 1 result from the oscillation of $\nabla^2\rho$ across the core electronic shells. As in the C–C bonded compounds, the valence region of the Laplacian features a prominent region of negative values in the internuclear space, reflecting a local concentration of electron density between the bonded atoms, as expected for a covalent bond. Also as expected, as bond order decreases, the magnitude of the negative Laplacian values in the internuclear region broadly decreases. In contrast to the symmetric $\nabla^2\rho$ curves for the C–C species (Figure 1B), those of the nitrogen-containing species are asymmetric. For NO^+, HNO, and H_2NOH, the local minimum proximal to the oxygen atom assumes more negative values than the local minimum proximal to the nitrogen. Moreover, whereas the $(3, -1)_\rho$ critical points of the C–C species are all coincident with the central local maximum of the $\nabla^2\rho$ curve (Figure 1B), the critical point occurs at differing locations along the $\nabla^2\rho$ curve for the different nitrogen compounds (Figure 3F–H). For NO^+, the critical point is nearly coincident with the local minimum proximal to the nitrogen, whereas for H_2NOH it is nearly at the local maximum. It is also noteworthy that the curves for H_3NOH^+ and H_3NO are even further skewed (Figure 3I–J); for the latter, the local minimum proximal to oxygen has almost vanished.

The $\nabla^2\rho$ curves for all the heavier pnictogen compounds feature a common pattern that is, as expected, distinct from that of the nitrogen compounds. A single local minimum exists and is

proximal to the oxygen. The presence of a single local minimum in $\nabla^2\rho$ along the bond path connecting second-period elements with third- or greater-period elements has been previously reported.[36-42] In the valence region, the value of $\nabla^2\rho$ rises from the oxygen-proximal minimum, passes through an inflection point near the midway point of the bond with $\nabla^2\rho \approx 0$, and then continues to increasingly positive values near the pnictogen. Among the phosphorus compounds, as the bond order decreases from PO^+ to HPO to H_2POH and H_3POH^+, the Laplacian curve progressively flattens in the vicinity of the inflection point. This flattening of the curve delays the onset of the rise to increasingly positive $\nabla^2\rho$ values proximal to the pnictogen and consequently, the value of $\nabla^2\rho_b$ gradually diminishes in magnitude, as captured in Figure 2B. A feature not captured by the $\nabla^2\rho_b$ values in Figure 2B is the decrease in the magnitude of the local minimum proximal to oxygen with decreasing bond order. Finally, the various H_2EOH and H_3EOH^+ series provide an opportunity to assess the influence of oxidation state on the Laplacian within a single bond type (nominal O–E single bond). The E(V) atoms have greater electronegativities than the corresponding E(III) atoms, resulting in a diminished electronegativity difference between the pnictogen and oxygen for H_3EOH^+ as compared to H_2EOH. As a result, the O–E bond in H_3EOH^+ would be expected to be more covalent. Although the differences between the compounds of the heavier elements are very small, we do indeed see this expected trend in the Laplacian, whereby that of H_3NOH^+ is more negative than that of H_2NOH at the $(3, -1)_\rho$ critical point (Figure 2B) or along the length of the bond path (Figure 3 H, I).

Within a given class of compounds, as the pnictogen becomes heavier, the $\nabla^2\rho$ curve generally shifts up and to the left, with both the oxygen-proximal minimum and inflection point occurring progressively closer to the oxygen atom (smaller normalized O–E distances) and progressively more positive $\nabla^2\rho$. We believe that the overall shape of the $\nabla^2\rho$ curve better

18

captures the variation that occurs across compound classes and element periods than the values

of $\nabla^2\rho_b$ alone. It is interesting to note that although $\nabla^2\rho_b$ for the singly-bonded Sb–O and Bi–O

species are similar to $\nabla^2\rho_b$ for the corresponding H_3EO compounds, the magnitude of the

oxygen-proximal $\nabla^2\rho$ minimum is greatly reduced for the latter. Given that monomeric stibine

oxides and bismuthine oxides are greatly underexplored as compared to compounds with Sb–O

and Bi–O single bonds, analysis of $\nabla^2\rho$ along the length of the bond path may discriminate

comparative stability and bond strength better than $\nabla^2\rho_b$.

In the case of ε, analysis along the full bond path (Figure 3 K–O) affords an opportunity

to understand the apparently counter-intuitive results provided by analysis of ε_b (*vide supra*). As

with ethyne (Table 1), the triple-bonded EO^+ molecules have $\varepsilon = 0$ along the entire length of the

bond path (Figure 3K). The spikes in the baseline appear to arise during the numerical processing

of the electron density data; note that they are absent from the DFT data in Figure S1 (*vide*

infra). For the HEO species, ε achieves a local maximum near the $(3, -1)_\rho$ critical point (Figure

3L). This maximum is bracketed by roots on either side. The curves also feature a prominent

oxygen-proximal maximum and a much smaller pnictogen-proximal maximum. The presence of

a local maximum near the $(3, -1)_\rho$ critical point is a featured shared by the ε curve for ethene

(Figure 1C). We note that the prominent oxygen- and pnictogen-proximal maxima in Figure 3L

occur in regions of the bond where $\nabla^2\rho$ has local minima (Figure 3G). This behavior has been

noted previously in polar bonds and has been ascribed to deviation of the eigenvector associated

with λ_2 from the plane of the molecule.[35,40] HNO, which has a well-defined nitrogen-proximal

minimum in $\nabla^2\rho$, features a correspondingly well-defined maximum in ε. In contrast, the HEO

compounds with heavier pnictogens, which do not feature a pnictogen-proximal valence

minimum in $\nabla^2\rho$, have ε values close to 0 in the pnictogen-proximal valence region. We also

highlight that, in general, the value of ε is expected to deviate from 0 in regions far from the $(3, -1)_\rho$ critical point of any bond if there is an asymmetric distribution of electron density around the atoms involved in that bond. For example, lone pairs on bonded atoms can skew electron density along a bond path from cylindrical symmetry proximal to that atom.

The singly-bonded H_2NOH and H_3NOH^+ also both feature maxima in ε near the regions where their $\nabla^2\rho$ curves have local minima. In contrast to HNO, however, ε for these two compounds reaches a value of zero between these maxima. This situation contrasts with that of ethane, for which ε = 0 along the length of the bond (Figure 1C). Nevertheless, for these O–N singly-bonded species, ε trends toward 0 in the vicinity of the $(3, -1)_\rho$ critical point. The fact that the $(3, -1)_\rho$ critical points for these molecules do not coincide exactly with their respective minima in ε explains the non-zero $ε_b$ values in Figure 2C and Table S2. The singly-bonded species of the heavier pnictogens feature a slightly different pattern. As with the nitrogen species, they feature a large maximum near the oxygen atom, where $\nabla^2\rho$ has a local minimum. As with the heavier HEO species, however, there is no prominent maximum in ε near the pnictogen (nor is there a corresponding pnictogen-proximal minimum in $\nabla^2\rho$). Moreover, unlike the nitrogen-containing species, the oxygen-proximal feature in ε for the heavier H_2EOH and H_3EOH^+ compounds bears a significant shoulder distal to the oxygen. For all compounds with E = P, As, Sb, or Bi, this shoulder extends into the vicinity of the $(3, -1)_\rho$ critical point before decaying to zero in the valence region of the pnictogen. The presence of this shoulder results in the non-zero values of $ε_b$ reported for these species in Figure 2C, and accounts for their deviation from the expected value of $ε_b \approx 0$. The steady migration of the critical point toward the oxygen as group 15 is descended results in $ε_b$ assuming progressively larger numbers, even surpassing those of the corresponding HEO species for E = Sb and Bi. The one apparent exception to the pattern is

H$_2$POH, which is in fact the only one of these compounds to show the expected $\varepsilon_b \approx 0$ in Figure 2C. Analysis of Figure 3M reveals that the overall form of the curve is the same as for the other compounds, but that the critical point happens to lie just outside of the shoulder.

The behavior of ε for the H$_3$EO compounds (Figure 3O), which are known to have bonds of order greater than 1,[25] highlights that this parameter does not report on bond order *per se* but rather on the preferential concentration of charge within a plane containing the bond. The ε value of 0 for the H$_3$EO compounds does not rule out a bond order greater than 1, but it does imply that any interactions additional to a single O–E bond are cylindrically symmetric. Previous orbital-based analyses of pnictine oxides of the general form X$_3$EO have suggested that donation from two orthogonal p-type lone pairs on the terminal oxygen atom into three E–X antibonding orbitals produces the characteristic strengthening of the O–E interaction, but maintains cylindrical symmetry about the O–E bond.[18] It is interesting to note that protonation of H$_3$EO to form H$_3$EOH$^+$ "ties up" one of these lone pairs, disrupting the cylindrical symmetry of the oxygen–pnictogen interaction as revealed by the behavior of ε along the bond path.

In summary, analysis of the patterns of ρ, $\nabla^2\rho$, and ε across the length of the bond path provides a means of differentiating different types of oxygen–pnictogen bonds and provides a richer source of information about chemical bonding than analysis of these functions at the $(3, -1)_\rho$ critical point alone. Analysis of ρ along the bond path reveals the asymmetry of the electron density distribution that is not captured by ρ_b. As expected on the basis of increasing orbital diffuseness as the family is descended, the asymmetry in ρ along the bond path decreases with increasing atomic number of E. Analysis of $\nabla^2\rho$ not only provides a better means of discriminating bond types than $\nabla^2\rho_b$, but it better captures the systematic variation in bonding across the compounds and periods. For example, charge concentration between the pnictogen

and oxygen across the entire valence region increases with bond order and decreases down the family, as expected from the increase in orbital overlap with bond order and the decrease in O–E orbital overlap as E becomes larger. Finally, the behavior of ε across the bond length provides an explanation for the seemingly counter-intuitive trends afforded by ε_b. Axially symmetric molecules (EO^+ and H_3EO) that feature cylindrically symmetric overlap of s and p orbitals along the O–E bond exhibit $\varepsilon = 0$ along the entire bond. The locally cylindrically symmetric overlap of atomic orbitals in molecules with O–E single bonds (H_2EOH and H_3EOH^+) results in ε reaching 0 in the valence region, although not necessarily at a location coincident with the $(3, -1)_\rho$ critical point. The lack of overall axial symmetry in these molecules relaxes the requirement that $\varepsilon = 0$ along the entire bond. The overlap of p-orbitals in the doubly-bonded HEO species results in accumulation of electron density above and below the plane of the molecule, and produces a maximum in ε in the vicinity of the $(3, -1)_\rho$ critical point. Because of the decreased propensity of heavier elements to engage in multiple bonding, the value of ε assumed at this local maximum decreases with increasing atomic number of E.

Extension to DFT methods. The analyses above revealed that the overall shapes of ρ, $\nabla^2\rho$, and ε along the bond path contain important information, but the electron densities used for these analyses were obtained at the computationally expensive orbital-optimized CCSD level of theory in an effort to best approximate the true electron density. We next sought to determine whether the patterns and trends observed above would persist robustly in analyses of electron densities obtained using computationally efficient DFT calculations of the sort typically employed for larger, more complex molecules. The progress of DFT has recently been criticized as deviating from the pursuit of the true electron density, but common hybrid functionals typically perform well in reproducing the densities of high-level correlated calculations.[48-53] The

geometries of the 25 compounds from Chart 1 were optimized at the PBE0/def2-TZVPP level of theory, which employs effective core potentials.[45] The electron densities were obtained at these optimized geometries with single-point energy second-order DKH calculations using the PBE0 functional and an all-electron, relativistically-contracted Ahlrichs-style triple-ζ basis set with extensive polarization functions. Electron densities were obtained for EO^+, HEO, H_2EOH, H_3EOH^+, and H_3EO with E = N, P, As, and Sb (Bi was not defined in the all-electron basis set used). Plots of ρ, $\nabla^2\rho$, and ε as a function of normalized O–E distance are presented in Figure S1 and recover all of the trends from Figure 3.

      Extension to organic derivatives. Having preliminarily validated the more scalable DFT methods, we next analyzed the topology of E–Me and E–Ph derivatives of two of the classes of compounds: H_3EO and H_3EOH^+. For the Me_3EO species (Figure 4A–B), the pattens in ρ and $\nabla^2\rho$ are essentially identical to those of the H_3EO species. For E = P, As, and Sb there is a single minimum in $\nabla^2\rho$ in the valence region proximal to the oxygen and the value of $\nabla^2\rho$ at this minimum is slightly more negative than for the corresponding H_3EO (Figure 4B). For H_3NO, the oxygen-proximal minimum in $\nabla^2\rho$ is essentially absent (Figure 3J), whereas for Me_3NO, it is slightly more pronounced (Figure 4B). The ε values are effectively zero along the lengths of the bonds of all of these cylindrically symmetric compounds (Figure 4C), although there are again spikes that arise during numerical processing of the data. For the singly-bonded cationic Me_3EOH^+ species, the situation again mirrors that of the H_3EOH^+ (Figure 4D-F). For Me_3NOH^+, there is a more pronounced oxygen-proximal minimum in $\nabla^2\rho$ than in Me_3NO and the absolute value of $\nabla^2\rho$ at the local maximum near the $(3, -1)_\rho$ critical point is smaller for the formally singly-bonded compound (Figure 4E). In Me_3NOH^+, the pnictogen-proximal minimum in $\nabla^2\rho$ is less negative than that of Me_3NO. Among the heavier pnictogens (E = P, As, Sb), the oxygen-

proximal minimum in $\nabla^2\rho$ is more negative for the Me_3EOH^+ compounds and in neither class of species is there a pnictogen-proximal minimum. The ε curve for Me_3NOH^+ exhibits two maxima near where $\nabla^2\rho$ features local valence minima. Between these maxima, ε descends to 0 near, but not coincident with, the $(3, -1)_\rho$ critical point (Figure 4F). The heavier Me_3EOH^+ species lack a pnictogen-proximal maximum in ε, and the oxygen-proximal feature has a significant shoulder that extends into the vicinity of the $(3, -1)_\rho$ critical point before diminishing to 0 near the pnictogen. Analogous results were obtained for the Ph_3EO and Ph_3EOH^+ compounds (Figure 4G-L). The patterns of these real-space functions (ρ, $\nabla^2\rho$, and ε) along the O–E bond paths of the organic-substituted species follow those established by the parent hydrides. These results indicate that this bond path analysis is applicable to organic EO derivatives only practically accessible with DFT calculations.
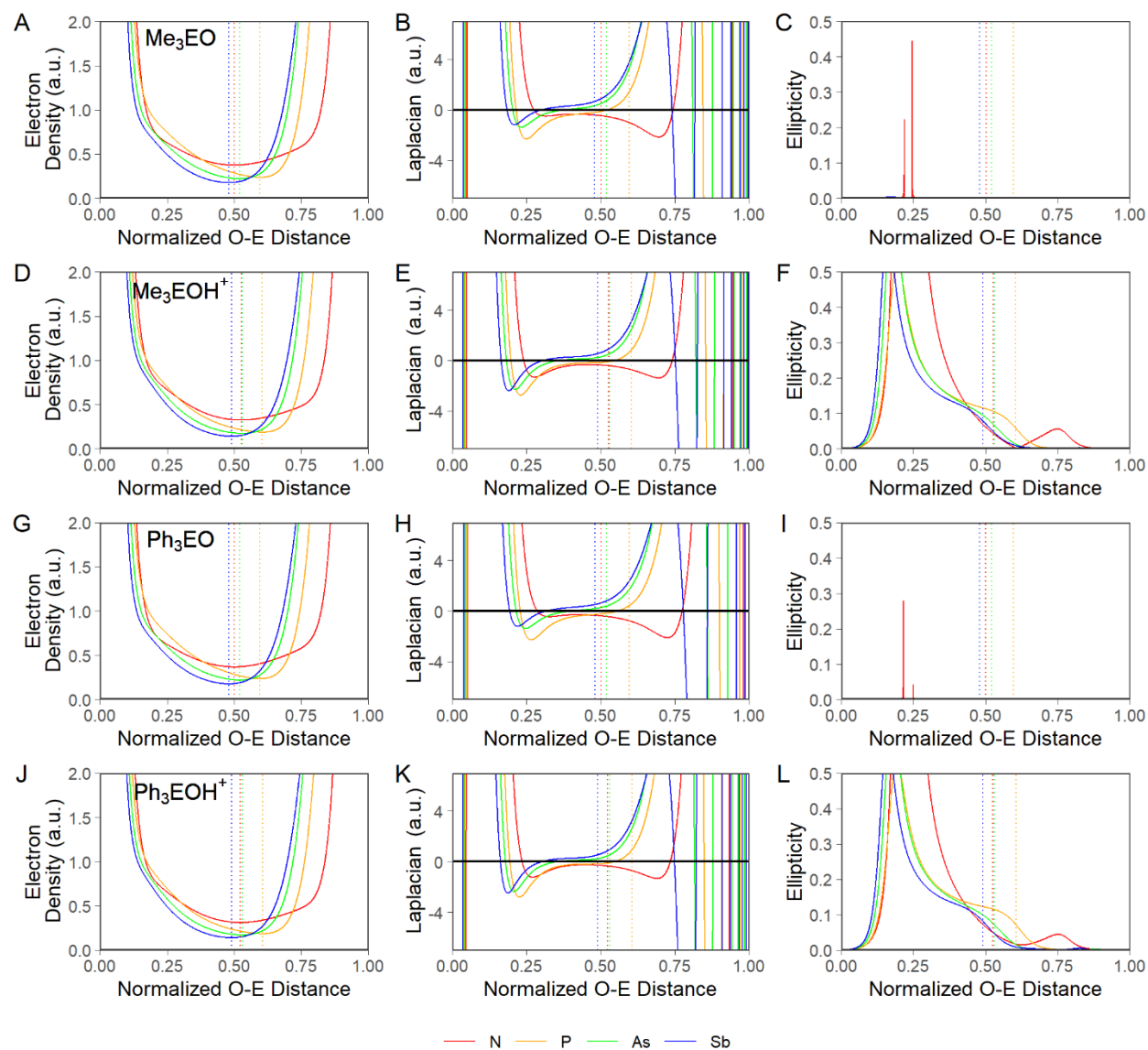
Figure 4. Evaluation (PBE0/old-DKH-TZVPP//PBE0/def2-TZVPP) of ρ, $\nabla^2\rho$, and ε along the normalized oxygen–pnictogen bond paths of different compounds (O at 0.0 and E and 1.0). Rows of panels feature data for a class of compounds: Me_3EO (A–C); Me_3EOH^+ (D–F); Ph_3EO (G–I); Ph_3EOH^+ (J–L); where E is a pnictogen. For (C) and (I), note that all compounds have $\varepsilon = 0$ along the length of the bond. Dashed vertical lines represent the location of the bond critical point. See Figure S5 for CVD balanced image.

CONCLUSIONS

The bonds formed between the pnictogens and oxygen are richly varied, exhibiting a range of geometric, electronic, and reactive properties. A number of different theoretical methods can be used to provide greater insight into the nature of the bonding interaction that exists between the pnictogen and oxygen in any given molecule and to discriminate between bond types. Here we have focused on the topological analysis of the electron density and its derivatives, which provides an orbital-agnostic means of analyzing electronic structure using only a physical observable: the electron density. Typical analyses of this sort rely on the evaluation of real-space functions such as ρ, $\nabla^2\rho$, and ε at the $(3, -1)_\rho$ critical point between the bonded atoms to provide information on the strength and nature of the bond. When performed on the oxygen–pnictogen bonded compounds described in this paper, such a classical analysis yielded unexpected trends, particularly in $\nabla^2\rho_b$ and ε_b of the compounds containing heavier pnictogens. We have demonstrated that analysis of these functions along the length of the bond path resolves the apparent discrepancies. While necessarily more information-rich, the full bond path analyses provide a set of simple patterns that are readily distinguishable to discriminate between bond types. The real-space function that perhaps performs best in this discriminatory capacity is ε. The formally O=E double-bonded species exhibit a local maximum near, but not necessarily coincident with, the $(3, -1)_\rho$ critical point. In contrast, for formally O–E single-bonded species, ε reaches 0 near, but not necessarily coincident with, the $(3, -1)_\rho$ critical point. For the heavier pnictogens, O–E single bonds exhibit a characteristic shoulder on the oxygen-proximal feature of the ε curve that proves particularly capable of obfuscating ε_b trends. Finally, the compounds with triple oxygen–pnictogen bonds or the partially multiply-bonded O=E/O$^-$–E$^+$

functional group of pnictine oxides investigated here were cylindrically symmetric and consequently ε was 0 along the length of the bond path. These two classes of compounds can, however, be readily distinguished by the behavior of $\nabla^2\rho_b$, which attains greater negative values at the oxygen-proximal local valence minimum for the triple bonds. These variations in behavior among the real-space functions can help to provide insight into the nature of the electronic structures of these compounds, but we anticipate that they will be most useful in helping to identify novel functional groups accessed by synthetic chemists, for we note that the organic derivatives of a number of these species have yet to be isolated.

COMPUTATIONAL METHODS

MP2 Geometry Optimization. All computational chemistry was performed using ORCA (version 4.2.1).[54,55] The geometries of the 25 panel compounds depicted in Chart 1 (EO$^+$, HEO, H$_2$EOH, H$_3$EOH$^+$ and H$_3$EO where E = N, P, As, Sb, or Bi) were optimized at the MP2/def2-QZVPP level of theory.[45] The resolution of the identity chain of spheres (RIJCOSX)[56] approximation was employed and the necessary auxiliary basis sets were generated using the AutoAux functionality.[57] Increased convergence criteria were employed during the SCF process (tightSCF) and the geometry optimization (tightOPT). The sizes of the integration grid and the COSX grid were increased (Grid7 GridX6 NOFINALGRID). The optimized coordinates are attached as Supporting Information.

CCSD Electron Density. Using the MP2/def2-QZVPP geometries (or literature geometries extracted from the NIST Computational Chemistry Comparison and Benchmark Database for ethane, ethene, ethyne, and Ne$_2$),[43] wavefunctions were obtained using atomic orbital coupled-

cluster singles doubles (AO-CCSD) calculations with an all-electron relativistically contracted quadruple-ζ atomic natural orbital (ANO-RCC-QZP)[46,47] basis set. The resolution of the identity approximation was employed (RI-AO) and relativistic effects were taken into consideration using the second-order Douglas-Kroll-Hess procedure (DKH). Orbital optimization, involving evaluation of the Z vector, was employed to obtain fully relaxed CCSD electron densities.

DFT calculations. The geometries of the nitrogen, phosphorus, arsenic, and antimony compounds in Chart 1 were optimized at the PBE0/def2-TZVPP level of theory,[45,58,59] employing the RIJCOSX approximation with the def2/J auxiliary basis set,[60] tight geometry optimization criteria (tightOPT), and expanded grids (Grid5 GridX7 NOFINALGRID). The electron density was then calculated at these optimized geometries using the hybrid PBE0 functional and an earlier version of the relativisitically contracted TZVPP basis set (old-DKH-TZVPP). The RIJCOSX approximation was employed with an appropriate segmented all-electron relativistically contracted (SARC/J)[61-64] auxiliary basis set. The second-order DKH method was used and expanded grids were employed (Grid7 GridX7 NOFINALGRID). Analogous DFT calculations were also performed on organic derivatives Me_3EO, Me_3EOH^+, Ph_3EO, and Ph_3EOH^+ where E = N, P, As, or Sb. The optimized coordinates are attached as Supporting Information.

Topological Analysis of Electron Density. The electron densities, either DFT or orbital-optimized CCSD, were analyzed using MultiWFN (version 3.7).[65] In all instances, a (3, −1) critical point in ρ was found between the oxygen and pnictogen (or pair of carbon or pair of neon) atoms. The values of ρ, $\nabla^2\rho$, and ε were either evaluated at the $(3, -1)_\rho$ critical point or along the length of the line connecting the oxygen and pnictogen (or pair of carbon or pair of neon) atoms. The values of these real-space functions along the interatomic line were further

analyzed using R (version 4.0.2) through RStudio (version 1.3.1073). The following R packages were used for analysis and visualization: tidyverse, gridExtra, ggtext, and grid. Color vision deficiency (CVD)-balanced images were generated using the *viridis* color map. Atomic charges were obtained by integrating electron densities across the atomic basins generated with a high-quality grid (0.06 bohr spacing) using MultiWFN. Integration was performed about the atomic center with uniform grids and exact refinement of the basin boundary.

ASSOCIATED CONTENT

Supporting Information. The following files are available free of charge.

Supplementary tables and figures (PDF)

Experimental Cartesian coordinates of reference compounds (XYZ)

MP2-optimized Cartesian coordinates of hydride derivatives (XYZ)

PBE0-optimized Cartesian coordinates of hydride derivatives (XYZ)

PBE0 optimized Cartesian coordinates of organic derivatives (XYZ)

AUTHOR INFORMATION

Corresponding Author

*Timothy C. Johnstone: johnstone@ucsc.edu

Author Contributions

The manuscript was written through contributions of all authors. All authors have given approval to the final version of the manuscript.

ABBREVIATIONS

ATP, adenosine triphosphate; ADP, adenosine diphosphate; MO, molecular orbital; NBO, natural bond orbital; HF, Hartree-Fock; DFT, density functional theory; AIM, Atoms in Molecules; QTAIM, Quantum Theory of Atoms in Molecules; ρ, electron density; $\nabla^2\rho$, Laplacian of the electron density; λ_n, n^{th} eigenvalue of the Hessian of ρ; $\nabla\rho$, gradient of ρ; ω, rank of critical point; σ, signature of critical point; ε, ellipticity; a.u., atomic units; CCSD, coupled cluster singles doubles; DKH, Douglas-Kroll-Hess; CVD, color vision deficiency.

REFERENCES

(1) Zhao, L.; Pan, S.; Holzmann, N.; Schwerdtfeger, P.; Frenking, G. Chemical Bonding and Bonding Models of Main-Group Compounds. *Chem. Rev.* **2019**, *119*, 8781-8845.

(2) Bayne, J. M.; Stephan, D. W. Phosphorus Lewis acids: emerging reactivity and applications in catalysis. *Chem. Soc. Rev.* **2016**, *45*, 765-774.

(3) Jones, J. S.; Gabbaï, F. P. Coordination- and Redox-Noninnocent Behavior of Ambiphilic Ligands Containing Antimony. *Acc. Chem. Res.* **2016**, *49*, 857-867.

(4) Cummins, C. C. Phosphorus: From the Stars to Land & Sea. *Daedalus* **2014**, *143*, 9-20.

(5) Robertson, A. P. M.; Gray, P. A.; Burford, N. Interpnictogen Cations: Exploring New Vistas in Coordination Chemistry. *Angew. Chem., Int. Ed.* **2014**, *53*, 6050-6069.

(6) Moc, J.; Morokuma, K. *Ab Initio* Molecular Orbital Study on the Periodic Trends in Structures and Energies of Hypervalent Compounds: Five-Coordinated XH_5 Species Containing a Group 15 Central Atom (X = P, As, Sb, and Bi). *J. Am. Chem. Soc.* **1995**, *117*, 11790-11797.

(7) Jerzembeck, W.; Bürger, H.; Constantin, L.; Margulès, L.; Demaison, J.; Breidung, J.; Thiel, W. Bismuthine BiH_3: Fact or Fiction? High-Resolution Infrared, Millimeter-Wave, and Ab Initio Studies. *Angew. Chem., Int. Ed.* **2002**, *41*, 2550-2552.

(8) Trubenstein, H. J.; Moaven, S.; Vega, M.; Unruh, D. K.; Cozzolino, A. F. Pnictogen bonding with alkoxide cages: which pnictogen is best? *New J. Chem.* **2019**, *43*, 14305-14312.

(9) Goicoechea, J. M.; Grützmacher, H. The Chemistry of the 2-Phosphaethynolate Anion. *Angew. Chem., Int. Ed.* **2018**, *57*, 16968-16994.

(10) Twamley, B.; Sofield, C. D.; Olmstead, M. M.; Power, P. P. Homologous Series of Heavier Element Dipnictenes 2,6-$Ar_2H_3C_6E$=EC_6H_3-2,6-Ar_2 (E = P, As, Sb, Bi; Ar = Mes = C_6H_2-2,4,6-Me_3; or Trip = C_6H2-2,4,6-$^iPr_3$) Stabilized by *m*-Terphenyl Ligands. *J. Am. Chem. Soc.* **1999**, *121*, 3357-3367.

(11) Greenwood, N. N.; Earnshaw, A. *Chemistry of the Elements*; 2nd ed.; Butterworth-Heinemann: Oxford ; Boston, 1997.

(12) Voet, D.; Voet, J. G. *Biochemistry*; 4th ed.; John Wiley & Sons: Hoboken, NJ, 2011.

(13) Gibaud, S.; Jaouen, G. Arsenic-Based Drugs: From Fowler's Solution to Modern Anticancer Chemotherapy, In *Medicinal Organometallic Chemistry*; Jaouen, G., Metzler-Nolte, N., (Eds.); Springer-Verlag: Berlin, 2010; Vol. 32, p 1-20.

(14) Nagle, A. S.; Khare, S.; Kumar, A. B.; Supek, F.; Buchynskyy, A.; Mathison, C. J. N.; Chennamaneni, N. K.; Pendem, N.; Buckner, F. S.; Gelb, M. H.; Molteni, V. Recent Developments in Drug Discovery for Leishmaniasis and Human African Trypanosomiasis. *Chem. Rev.* **2014**, *114*, 11305-11347.

(15) Andrews, P. C.; Deacon, G. B.; Forsyth, C. M.; Junk, P. C.; Kumar, I.; Maguire, M. Towards a Structural Understanding of the Anti-Ulcer and Anti-Gastritis Drug Bismuth Subsalicylate. *Angew. Chem., Int. Ed.* **2006**, *45*, 5638-5642.

(16) Rogachev, A. Yu.; Burger, P. Bonding situation and N–O-bond strengths in amine-*N*-oxides—a combined experimental and theoretical study. *Phys. Chem. Chem. Phys.* **2012**, *14*, 1985–2000.

(17) Łukomska, M.; Rybarczyk-Pirek, A. J.; Jabłoński, M.; Palusiak, M. The nature of NO-bonding in *N*-oxide group. *Phys. Chem. Chem. Phys.* **2015**, *17*, 16375-16387.

(18) Dobado, J. A.; Martínez-García, H.; Molina; Sundberg, M. R. Chemical Bonding in Hypervalent Molecules Revised. Application of the Atoms in Molecules Theory to Y_3X and Y_3XZ (Y = H or CH_3; X = N, P or As; Z = O or S) Compounds. *J. Am. Chem. Soc.* **1998**, *120*, 8461-8471.

(19) Chesnut, D. B.; Savin, A. The Electron Localization Function (ELF) Description of the PO Bond in Phosphine Oxide. *J. Am. Chem. Soc.* **1999**, *121*, 2335-2336.

(20) Lyssenko, K. A.; Grintselev-Knyazev, G. V.; Antipin, M. Y. Nature of the PO bond in diphenylphosphonic acid: experimental charge density and electron localization function analysis. *Mendeleev Commun.* **2002**, *12*, 128-130.

(21) Chesnut, D. B. Atoms-in-Molecules and Electron Localization Function Study of the Phosphoryl Bond. *J. Phys. Chem. B* **2003**, *107*, 4307-4313.

(22) Gamoke, B.; Neff, D.; Simons, J. Nature of PO Bonds in Phosphates. *J. Phys. Chem. B* **2009**, *113*, 5677-5684.

(23) Yamada, K.; Koga, N. Variationally determined electronic states for the theoretical analysis of intramolecular interaction. II. Qualitative nature of the P—O bond in phosphine oxides. *J. Comput. Chem.* **2013**, *34*, 149-161.

(24) Viana, R. B. Tailoring the electronic properties among oxoarsine, arsinoyl and arsine oxide isomers: the simplest molecular systems with an arsenic–oxygen bond. *RSC Adv.* **2016**, *6*, 90760-90770.

(25) Yang, T.; Andrada, D. M.; Frenking, G. Dative versus electron-sharing bonding in N-oxides and phosphane oxides R_3EO and relative energies of the R_2EOR isomers (E = N, P; R = H, F, Cl, Me, Ph). A theoretical study. *Phys. Chem. Chem. Phys.* **2018**, *20*, 11856-11866.

(26) Glendening, E. D.; Landis, C. R.; Weinhold, F. NBO 7.0: New vistas in localized and delocalized chemical bonding theory. *J. Comput. Chem.* **2019**, *40*, 2234–2241.

(27) Stowasser, R.; Hoffmann, R. What Do the Kohn−Sham Orbitals and Eigenvalues Mean? *J. Am. Chem. Soc.* **1999**, *121*, 3414-3420.

(28) Bader, R. F. W. Atoms in molecules. *Acc. Chem. Res.* **1985**, *18*, 9-15.

(29) Bader, R. F. W. A quantum theory of molecular structure and its applications. *Chem. Rev.* **1991**, *91*, 893-928.

(30) Bader, R. F. W. A Bond Path: A Universal Indicator of Bonded Interactions. *J. Phys. Chem. B* **1998**, *102*, 7314-7323.

(31) Danovich, D.; Shaik, S.; Rzepa, H. S.; Hoffmann, R. A Response to the Critical Comments on "One Molecule, Two Atoms, Three Views, Four Bonds?". *Angew. Chem., Int. Ed.* **2013**, *52*, 5926-5928.

(32) Bader, R. F. W.; Essén, H. The characterization of atomic interactions. *J. Chem. Phys.* **1984**, *80*, 1943-1960.

(33) Bader, R. F. W.; Slee, T. S.; Cremer, D.; Kraka, E. Description of conjugation and hyperconjugation in terms of electron distributions. *J. Am. Chem. Soc.* **1983**, *105*, 5061-5068.

(34) Cremer, D.; Kraka, E.; Slee, T. S.; Bader, R. F. W.; Lau, C. D. H.; Nguyen Dang, T. T.; MacDougall, P. J. Description of homoaromaticity in terms of electron distributions. *J. Am. Chem. Soc.* **1983**, *105*, 5069-5075.

(35) Cheeseman, J. R.; Carroll, M. T.; Bader, R. F. W. The mechanics of hydrogen bond formation in conjugated systems. *Chem. Phys. Lett.* **1988**, *143*, 450-458.

(36) Scherer, W.; Sirsch, P.; Grosche, M.; Spiegler, M.; Mason, S. A.; Gardiner, M. G. Agostic deformations based on electron delocalization in the alkyllithium-complex [{2-$(Me_3Si)_2CLiC_5H_4N$}$_2$. *Chem. Commun.* **2001**, 2072-2073.

(37) Scherer, W.; Sirsch, P.; Shorokhov, D.; McGrady, G. S.; Mason, S. A.; Gardiner, M. G. Valence-Shell Charge Concentrations and Electron Delocalization in Alkyllithium Complexes: Negative Hyperconjugation and Agostic Bonding. *Chem.–Eur. J.* **2002**, *8*, 2324-2334.

(38) Tafipolsky, M.; Scherer, W.; Öfele, K.; Artus, G.; Pedersen, B.; Herrmann, W. A.; McGrady, G. S. Electron Delocalization in Acyclic and *N*-Heterocyclic Carbenes and Their Complexes: A Combined Experimental and Theoretical Charge-Density Study. *J. Am. Chem. Soc.* **2002**, *124*, 5865-5880.

(39) Ott, H.; Däschlein, C.; Leusser, D.; Schildbach, D.; Seibel, T.; Stalke, D.; Strohmann, C. Structure/Reactivity Studies on an α-Lithiated Benzylsilane: Chemical Interpretation of Experimental Charge Density. *J. Am. Chem. Soc.* **2008**, *130*, 11901-11911.

(40) Farrugia, L. J.; Khalaji, A. D. Evidence for Side-Chain π-Delocalization in a Planar Substituted Benzene: An Experimental and Theoretical Charge Density Study on 2,5-Dimethoxybenzaldehyde Thiosemicarbazone. *J. Phys. Chem. B* **2011**, *115*, 12512-12522.

(41) Huang, W. J.; Momen, R.; Azizi, A.; Xu, T.; Kirk, S. R.; Filatov, M.; Jenkins, S. Next-generation quantum theory of atoms in molecules for the ground and excited states of fulvene. *Int. J. Quantum Chem.* **2018**, *118*, e25768.

(42) Espinosa Ferao, A.; García Alcaraz, A.; Zaragoza Noguera, S.; Streubel, R. Terminal Phosphinidene Complex Adducts with Neutral and Anionic O-Donors and Halides and the Search for a Differentiating Bonding Descriptor. *Inorg. Chem.* **2020**, *59*, 12829-12841.

(43) NIST Computational Chemistry Comparison and Benchmark Database; NIST Standard Reference Database Number 101, Realease 21 (August 2020), <http://cccbdb.nist.gov/>

(44) Ulrich, B.; Vredenborg, A.; Malakzadeh, A.; Schmidt, L. P. H.; Havermeier, T.; Meckel, M.; Cole, K.; Smolarski, M.; Chang, Z.; Jahnke, T.; Dörner, R. Imaging of the Structure of the Argon and Neon Dimer, Trimer, and Tetramer. *J. Phys. Chem. B* **2011**, *115*, 6936-6941.

(45) Weigend, F.; Ahlrichs, R. Balanced basis sets of split valence, triple zeta valence and quadruple zeta valence quality for H to Rn: Design and assessment of accuracy. *Phys. Chem. Chem. Phys.* **2005**, *7*, 3297-3305.

(46) Widmark, P.-O.; Malmqvist, P.-Å.; Roos, B. O. Density matrix averaged atomic natural orbital (ANO) basis sets for correlated molecular wave functions. *Theor. Chim. Acta* **1990**, *77*, 291-306.

(47) Roos, B. O.; Lindh, R.; Malmqvist, P.-Å.; Veryazov, V.; Widmark, P.-O. Main Group Atoms and Dimers Studied with a New Relativistic ANO Basis Set. *J. Phys. Chem. B* **2004**, *108*, 2851-2858.

(48) Medvedev, M. G.; Bushmarinov, I. S.; Sun, J.; Perdew, J. P.; Lyssenko, K. A. Density functional theory is straying from the path toward the exact functional. *Science* **2017**, *355*, 49-52.

(49) Kepp, K. P. Comment on "Density functional theory is straying from the path toward the exact functional". *Science* **2017**, *356*, 496b.

(50) Brorsen, K. R.; Yang, Y.; Pak, M. V.; Hammes-Schiffer, S. Is the Accuracy of Density Functional Theory for Atomization Energies and Densities in Bonding Regions Correlated? *J. Phys. Chem. Lett.* **2017**, *8*, 2076-2081.

(51) Medvedev, M. G.; Bushmarinov, I. S.; Sun, J.; Perdew, J. P.; Lyssenko, K. A. Response to Comment on "Density functional theory is straying from the path toward the exact functional". *Science* **2017**, *356*, 496c.

(52) Ranasinghe, D. S.; Perera, A.; Bartlett, R. J. A note on the accuracy of KS-DFT densities. *J. Chem. Phys.* **2017**, *147*, 204103.

(53) Mayer, I.; Pápai, I.; Bakó, I.; Nagy, Á. Conceptual Problem with Calculating Electron Densities in Finite Basis Density Functional Theory. *J. Chem. Theory Comput.* **2017**, *13*, 3961-3963.

(54) Neese, F. The ORCA program system. *WIREs Computational Molecular Science* **2011**, *2*, 73-78.

(55) Neese, F. Software update: the ORCA program system, version 4.0. *WIREs Computational Molecular Science* **2018**, *8*, e1327.

(56) Kossmann, S.; Neese, F. Efficient Structure Optimization with Second-Order Many-Body Perturbation Theory: The RIJCOSX-MP2 Method. *J. Chem. Theory Comput.* **2010**, *6*, 2325-2338.

(57) Stoychev, G. L.; Auer, A. A.; Neese, F. Automatic Generation of Auxiliary Basis Sets. *J. Chem. Theory Comput.* **2017**, *13*, 554-562.

(58) Perdew, J. P.; Ernzerhof, M.; Burke, K. Rationale for mixing exact exchange with density functional approximations. *J. Chem. Phys.* **1996**, *105*, 9982-9985.

(59) Perdew, J. P.; Burke, K.; Ernzerhof, M. Generalized Gradient Approximation Made Simple. *Phys. Rev. Lett.* **1996**, *77*, 3865-3868.

(60) Weigend, F. Accurate Coulomb-fitting basis sets for H to Rn. *Phys. Chem. Chem. Phys.* **2006**, *8*, 1057-1065.

(61) Pantazis, D. A.; Chen, X.-Y.; Landis, C. R.; Neese, F. All-Electron Scalar Relativistic Basis Sets for Third-Row Transition Metal Atoms. *J. Chem. Theory Comput.* **2008**, *4*, 908-919.

(62) Pantazis, D. A.; Neese, F. All-Electron Scalar Relativistic Basis Sets for the Lanthanides. *J. Chem. Theory Comput.* **2009**, *5*, 2229-2238.

(63) Pantazis, D. A.; Neese, F. All-Electron Scalar Relativistic Basis Sets for the Actinides. *J. Chem. Theory Comput.* **2011**, *7*, 677-684.

(64) Pantazis, D. A.; Neese, F. All-electron scalar relativistic basis sets for the 6p elements. *Theor. Chem. Acc.* **2012**, *131*, 1292.

(65) Lu, T.; Chen, F. Multiwfn: A multifunctional wavefunction analyzer. *J. Comput. Chem.* **2012**, *33*, 580-592.

SYNOPSIS

Topological analysis of electron density is used with increasing frequency to shed light on the bonding in inorganic compounds. Such analyses typically rely on an assessment of different real-space functions (e.g., ρ, $\nabla^2\rho$, and ε) at the bond critical point. We demonstrate here that such an analysis provides misleading results across a series of oxygen–pnictogen bonded compounds but that analysis of these functions across the length of the bond path resolves the discrepancies.

TOC GRAPIC

Pnictogen–Oxygen Polar Covalent Bonding
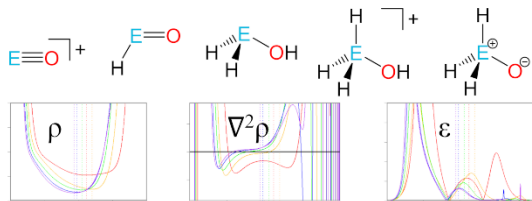
Bond Critical Point Analysis ➔ confounding trends ✗
Full Bond Path Analysis ➔ consistent trends ✓

Supporting Information for:

Analysis of Oxygen–Pnictogen Bonding with Full Bond Path Topological Analysis of the Electron Density

Brent Lindquist-Kleissler, John S. Wenger, and Timothy C. Johnstone*

Department of Chemistry and Biochemistry, University of California, Santa Cruz, Santa Cruz, California 95064, United States.

* johnstone@ucsc.edu

CONTENTS

Table S1. Comparison of Computationally and Experimentally Determined Geometric Parameters for O–E Compounds Under Investigation

Compound	Experimental O–E Bond Length (Å)	Method and Reference	MP2/def2-QZVPP Calculated O–E Bond Length (Å)	PBE0/def2-TZVPP Calculated O–E Bond Length (Å)
NO^+	1.062(4)	X-ray crystallography[1] IF_5 cocrystal of NO_3^- salt	1.079	1.054
	1.063250(24)	Photoelectron spectroscopy[2] (r_e)		
PO^+	1.4249927(4)	Microwave spectroscopy[3] (r_e)	1.445	1.420
	1.419(5)	Photoelectron spectroscopy[4] (r_e)		
AsO^+	1.568*	UV spectroscopy[5] (r_e)	1.589	1.557
SbO^+	1.8074*	UV spectroscopy[6] (r_e)	1.795	1.752
HNO	1.211(6)	Microwave spectroscopy[7] (r_0)	1.217	1.190
	1.20880(2)	Millimeterwave spectroscopy[8] ($r_m^{(1)}$)		
HPO	1.4801(1)	Laser-induced fluorescence[9] (r_e)	1.493	1.478
	1.4800(9)	Microwave spectroscopy[10] (r_e)		
HAsO	1.6342(5)	Laser-induced fluorescence[11] (r_0)	1.641	1.622
	1.631*	Estimated[12] r_e using r_0 value from ref 11 and MRCI-F12/CVQZ-F12 potential energy functions		
H_2NOH	1.47(3)	X-ray crystallography[13]	1.436	1.423
	1.453(2)	Microwave spectroscopy[14]		
H_3NOH^+	1.411(2)	X-ray crystallography[15] of chloride salt	1.393	1.385
H_3PO	1.4763*	Microwave spectroscopy[16] (r_0)	1.479	1.474

* No experimental error reported in reference.

Table S2. Numerical Values of ρ_b, $\nabla^2\rho_b$, and ε_b Depicted in Figure 2

	ρ_b (a.u.)	$\nabla^2\rho_b$ (a.u.)	ε_b
NO^+	0.747	-3.538	0.000
PO^+	0.257	1.869	0.000
AsO^+	0.245	1.076	0.000
SbO^+	0.189	0.827	0.000
BiO^+	0.174	0.646	0.000
HNO	0.521	-1.548	0.113
HPO	0.232	1.381	0.129
HAsO	0.218	0.766	0.091
HSbO	0.173	0.672	0.063
HBiO	0.157	0.527	0.058
H_2NOH	0.298	-0.398	0.027
H_2POH	0.163	0.542	0.002
H_2AsOH	0.154	0.360	0.040
H_2SbOH	0.128	0.424	0.065
H_2BiOH	0.115	0.358	0.074
H_3NOH^+	0.347	-0.637	0.055
H_3POH^+	0.207	0.935	0.080
H_3AsOH^+	0.194	0.528	0.072
H_3SbOH^+	0.157	0.559	0.084
H_3BiOH^+	0.142	0.423	0.088
H_3NO	0.366	-0.442	0.000
H_3PO	0.243	1.375	0.000
H_3AsO	0.229	0.609	0.000
H_3SbO	0.183	0.598	0.000
H_3BiO	0.168	0.452	0.000

Table S3. AIM Atomic Charges (CCSD/ANO-RCC-QZP//MP2/def2-QZVPP)

|	Charge on O	Charge on E	Charge separation
NO^+	-0.30	1.30	1.60
PO^+	-1.20	2.20	3.41
AsO^+	-0.83	1.83	2.66
SbO^+	-0.86	1.86	2.73
BiO^+	-0.79	1.79	2.57
HNO	-0.42	0.10	0.52
HPO	-1.39	2.02	3.41
HAsO	-1.04	1.39	2.44
HSbO	-1.06	1.46	2.51
HBiO	-0.96	1.31	2.28
H_2NOH	-0.85	-0.54	0.31
H_2POH	-1.44	2.03	3.46
H_2AsOH	-1.26	1.28	2.54
H_2SbOH	-1.27	1.41	2.68
H_2BiOH	-1.23	1.27	2.50
H_3NOH^+	-0.72	-0.65	0.07
H_3POH^+	-1.52	3.51	5.03
H_3AsOH^+	-1.28	2.18	3.47
H_3SbOH^+	-1.30	2.36	3.66
H_3BiOH^+	-1.23	1.94	3.17
H_3NO	-0.71	-0.52	0.19
H_3PO	-1.57	3.46	5.03
H_3AsO	-1.19	2.07	3.27
H_3SbO	-1.18	2.18	3.36
H_3BiO	-1.04	1.77	2.81
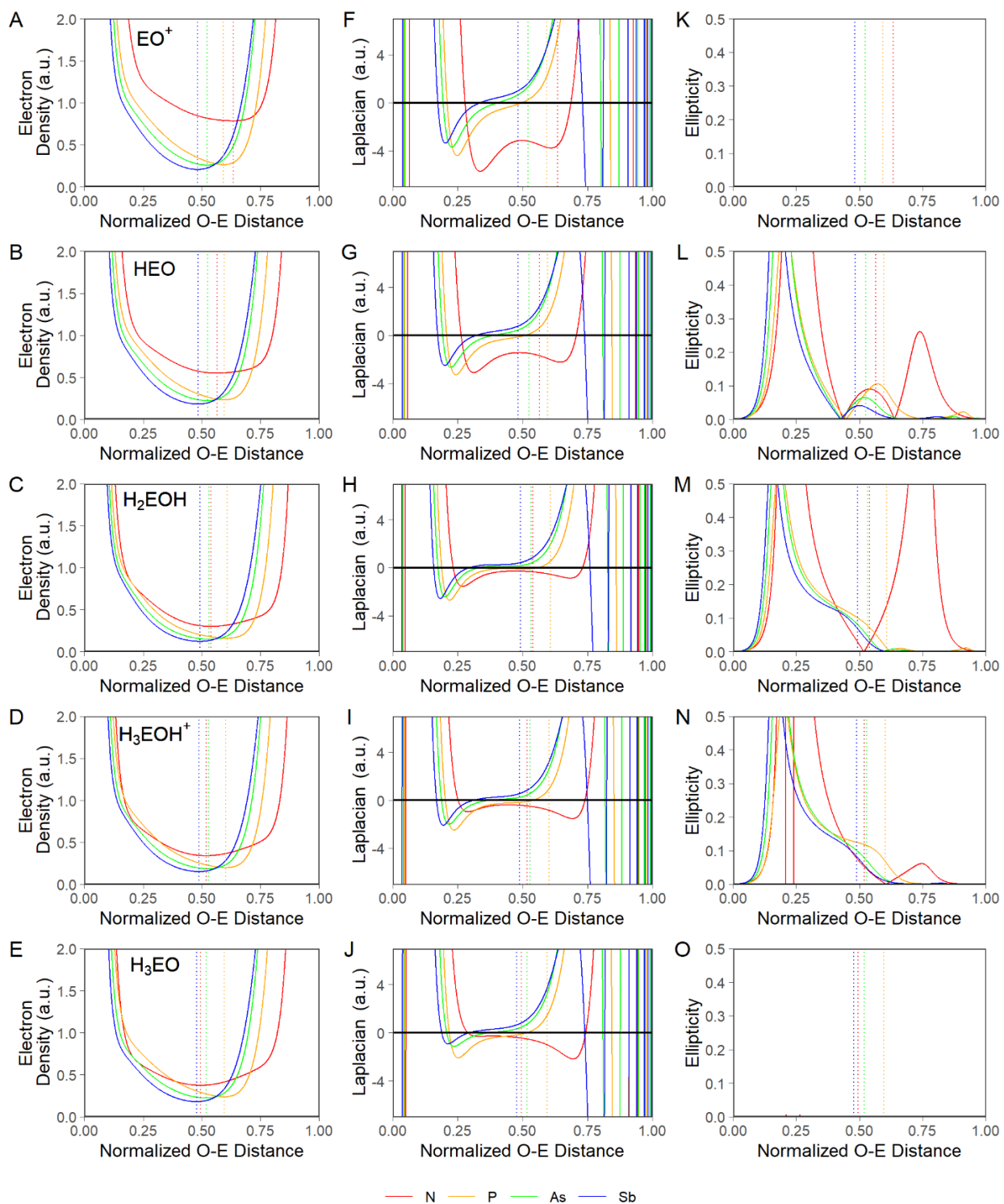
Figure S1. Evaluation (PBE0-DKH/old-DKH-TZVPP//PBE0/def2-TZVPP) of electron density, Laplacian, and ellipticity along the normalized oxygen–pnictogen bond paths of different compounds (O at 0.0 and E and 1.0). Rows of panels feature data for a class of compounds: EO^+ (A, F, K); HEO (B, G, L); H_2EOH (C, H, M); H_3EOH^+ (D, I, N); and H_3EO (E, J, O) where E is a pnictogen. For (K) and (O), note that all compounds have $\varepsilon = 0$ along the length of the bond. Dashed vertical lines represent the location of the bond critical point. See Figure S6 for color vision deficiency (CVD) balanced image.
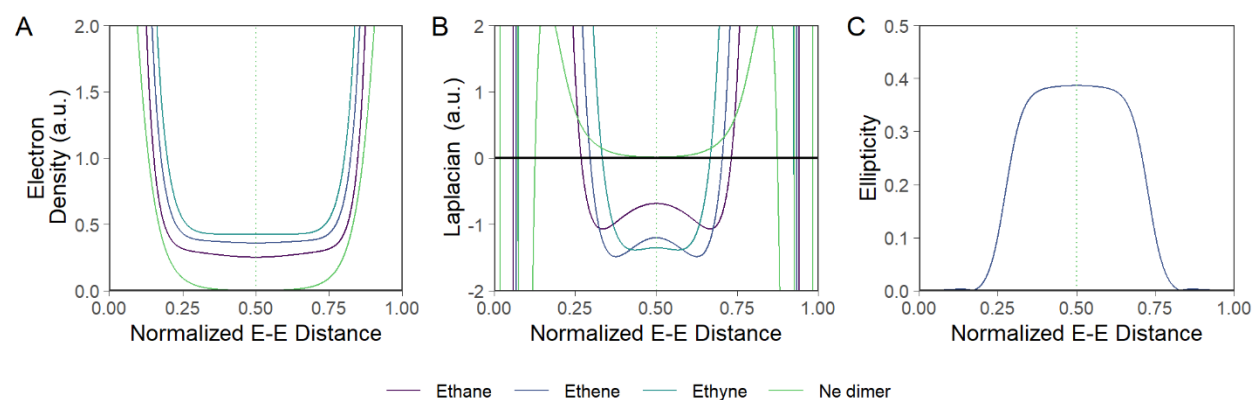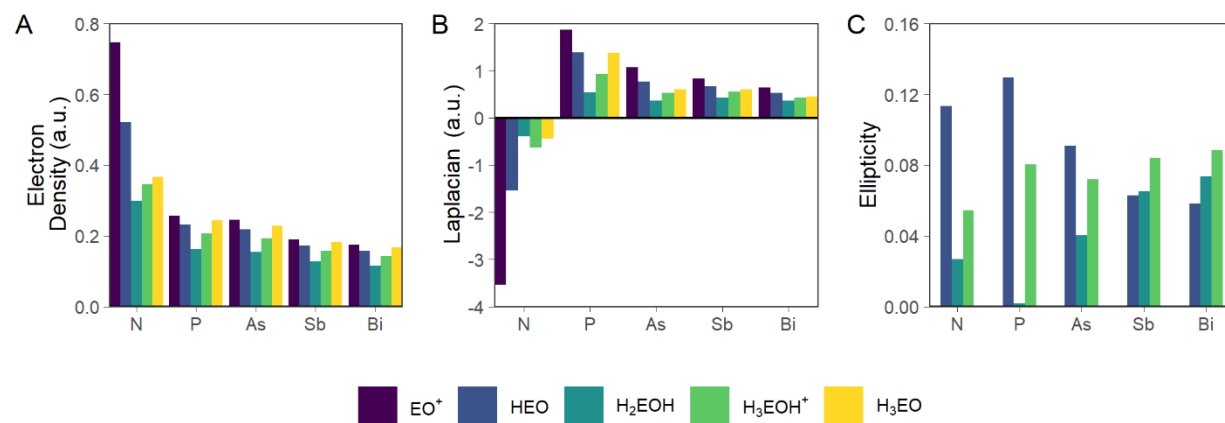
Figure S2. Reproduction of Figure 1 with a color scheme balanced for color vision deficiency. Plots of (A) ρ, (B) $\nabla^2\rho$, and (C) ε as a function of the normalized C–C (for ethane, ethene, and ethyne) or Ne–Ne (for Ne dimer) bond length for a series of reference compounds. For (C), note that ethane, ethyne, and Ne_2 have $\varepsilon = 0$ along the length of the bond. Orbital-optimized electron densities were obtained from single-point CCSD/ANO-RCC-QZP calculations at experimental geometries extracted from the NIST CCCDB.[43]

Figure S3. Reproduction of Figure 2 with a color scheme balanced for color vision deficiency. Values of (A) ρ_b, (B) $\nabla^2\rho_b$, and (C) ε_b for all 15 species grouped by pnictogen and colored by compound type. For (C), note that all EO^+ and H_3EO compounds have $\varepsilon_b = 0$. Note that ρ_b, $\nabla^2\rho_b$, and ε_b are the values of ρ, $\nabla^2\rho$, and ε at the (3,–1) critical point in ρ.
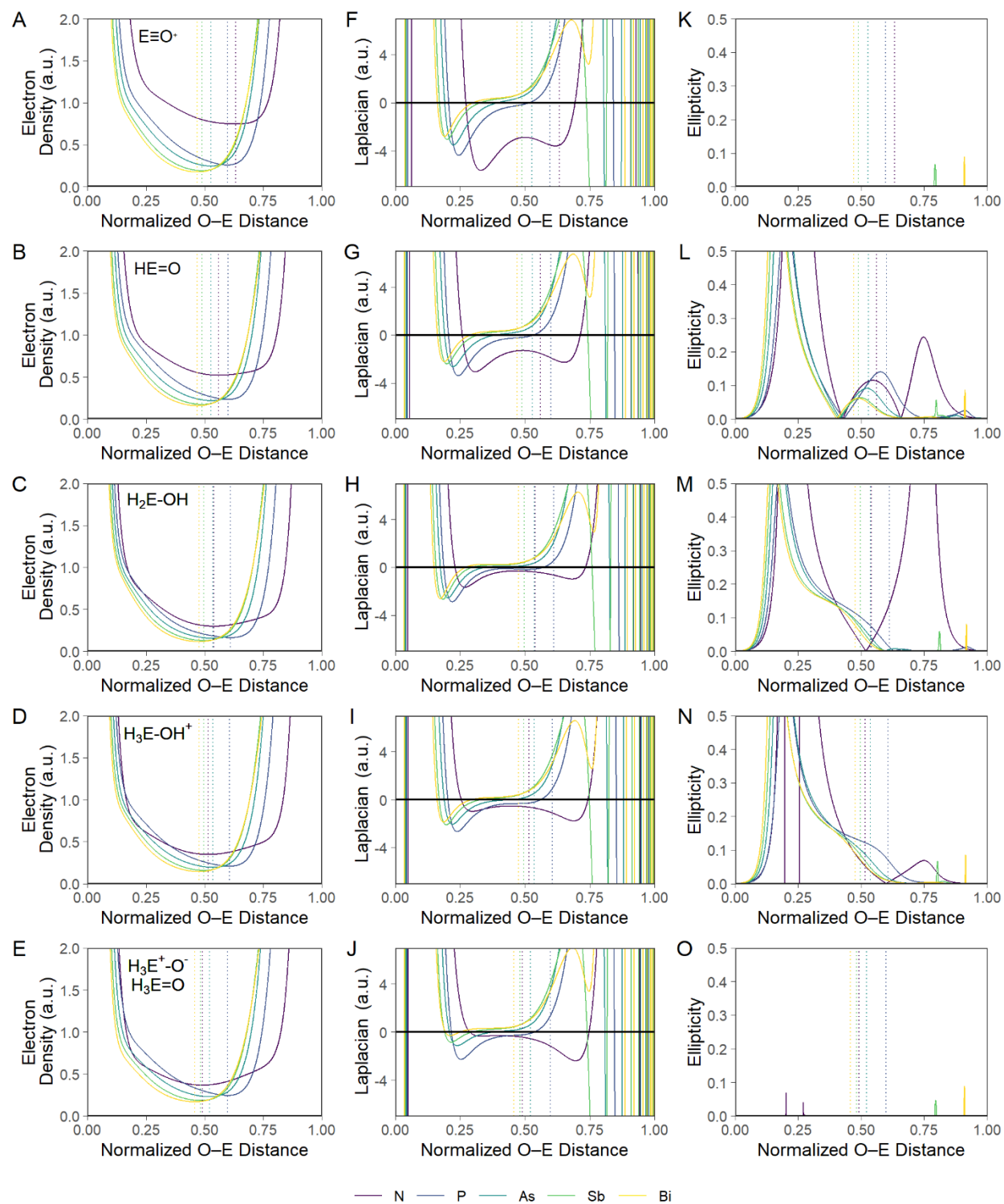
Figure S4. Reproduction of Figure 3 with a color scheme balanced for color vision deficiency. Evaluation (CCSD/ANO-RCC-QZP//MP2/def2-QZVPP) of electron density, Laplacian, and ellipticity along the normalized oxygen–pnictogen bond paths of different compounds (O at 0.0 and E and 1.0). Rows of panels feature data for a class of compounds: EO^+ (A, F, K); HEO (B, G, L); H_2EOH (C, H, M); H_3EOH^+ (D, I, N); and H_3EO (E, J, O) where E is a pnictogen. For (K) and (O), note that all compounds have $\varepsilon = 0$ along the length of the bond. Dashed vertical lines represent the location of the bond critical point.
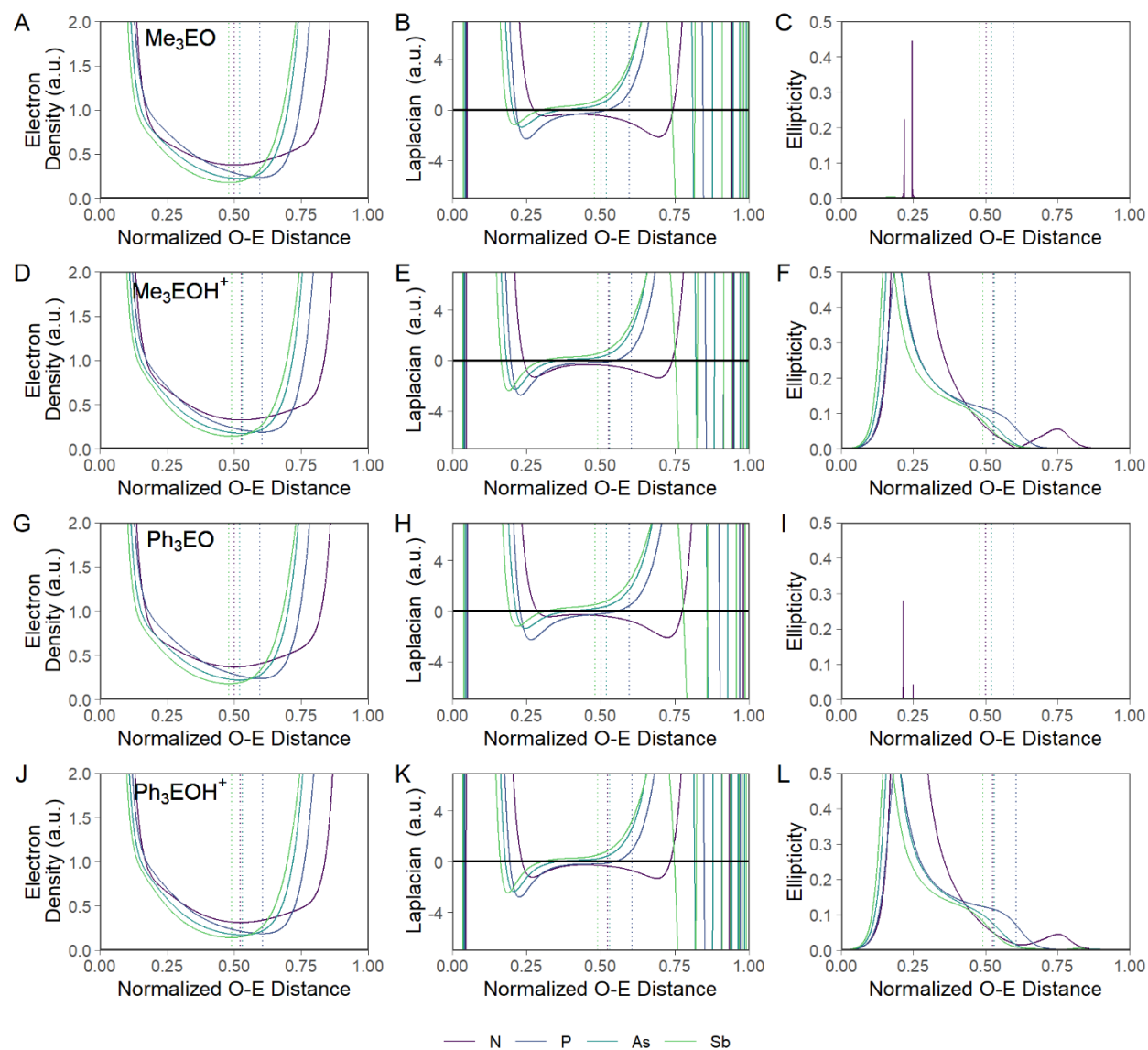
Figure S5. Reproduction of Figure 4 with a color scheme balanced for color vision deficiency. Evaluation (PBE0/old-DKH-TZVPP//PBE0/def2-TZVPP) of ρ, $\nabla^2\rho$, and ε along the normalized oxygen–pnictogen bond paths of different compounds (O at 0.0 and E and 1.0). Rows of panels feature data for a class of compounds: Me$_3$EO (A–C); Me$_3$EOH$^+$ (D–F); Ph$_3$EO (G–I); Ph$_3$EOH$^+$ (J–L); where E is a pnictogen. For (C) and (I), note that all compounds have $\varepsilon = 0$ along the length of the bond. Dashed vertical lines represent the location of the bond critical point.
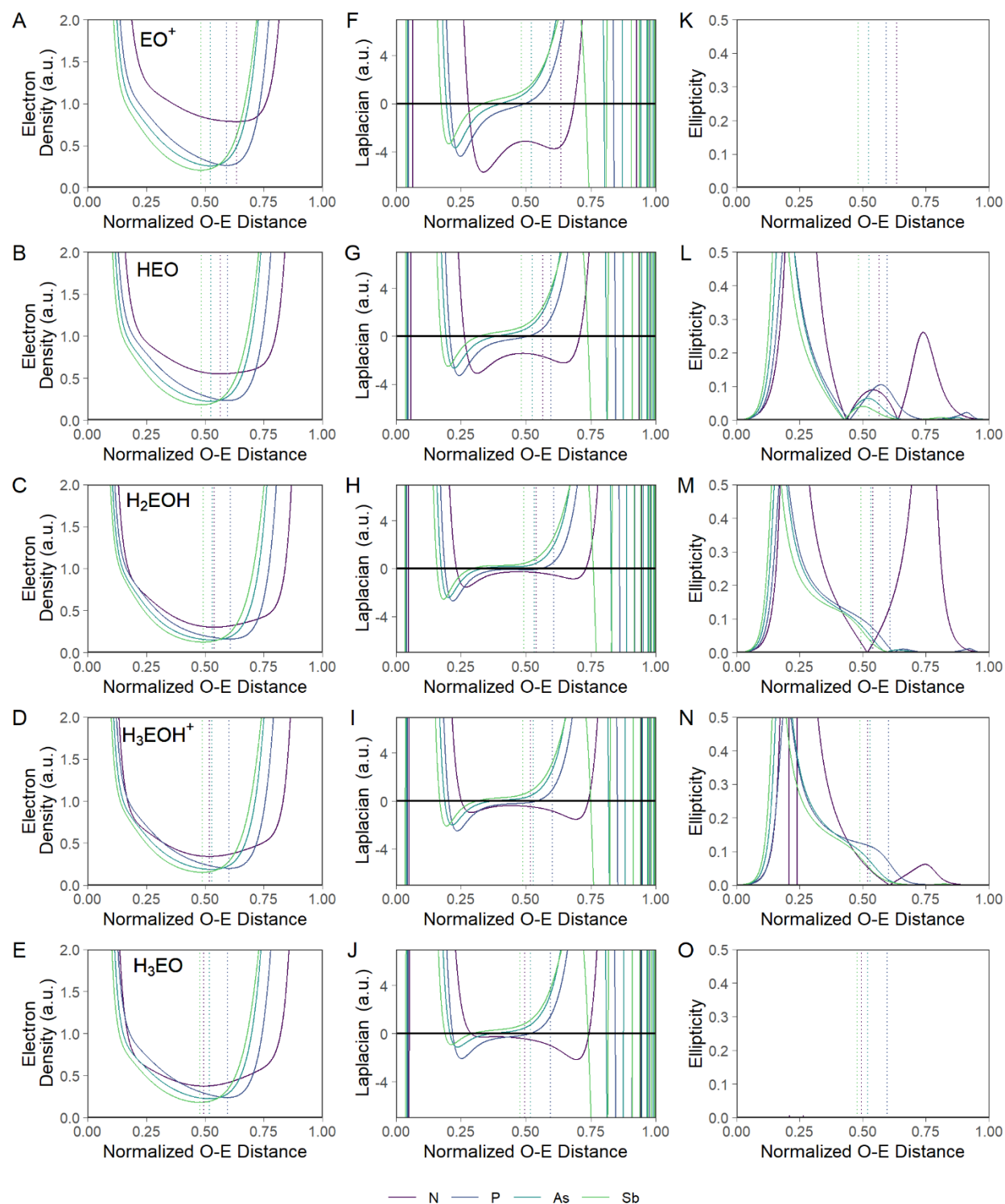
Figure S6. Reproduction of Figure S1 with a color scheme balanced for color vision deficiency. Evaluation (PBE0-DKH/old-DKH-TZVPP//PBE0/def2-TZVPP) of electron density, Laplacian, and ellipticity along the normalized oxygen–pnictogen bond paths of different compounds (O at 0.0 and E and 1.0). Rows of panels feature data for a class of compounds: EO$^+$ (A, F, K); HEO (B, G, L); H_2EOH (C, H, M); H_3EOH^+ (D, I, N); and H_3EO (E, J, O) where E is a pnictogen. For (K) and (O), note that all compounds have $\varepsilon = 0$ along the length of the bond. Dashed vertical lines represent the location of the bond critical point.

REFERENCES

(1) Zhang, X.; Seppelt, K. Nitrosonium Nitrate, an Isomer of N_2O_4 in IF_5. *Z. Anorg. Allg. Chem.* **1998**, *624*, 667-670.

(2) Albritton, D. L.; Schmeltekopf, A. L.; Zare, R. N. Potential energy curves for NO^+. *J. Chem. Phys.* **1979**, *71*, 3271-3279.

(3) Petrmichl, R. H.; Peterson, K. A.; Woods, R. C. The microwave spectrum of PO^+: Comparison to SiF^+. *J. Chem. Phys.* **1991**, *94*, 3504-3510.

(4) Dyke, J. M.; Morris, A.; Ridha, A. Study of the ground state of PO^+ using photoelectron spectroscopy. *J. Chem. Soc., Faraday Trans. 2* **1982**, *78*, 2077-2082.

(5) Rao, D. V. K.; Rao, P. T. Rotational analysis of the ultra-violet system of AsO^+. *J. Phys. B: At. Mol. Phys.* **1970**, *3*, 430-437.

(6) Tripathi, R.; Rai, S. B.; Upadhya, K. N. The A-X system of the SbO^+ molecule. *J. Phys. B: At. Mol. Phys.* **1981**, *14*, 441-445.

(7) Saito, S.; Takagi, K. Microwave spectrum of nitroxyl. *J. Mol. Spectrosc.* **1973**, *47*, 99-106.

(8) Zaleski, D. P.; Prozument, K. Pseudo-equilibrium geometry of HNO determined by an E-Band CP-FTmmW spectrometer. *Chem. Phys. Lett.* **2017**, *680*, 101-108.

(9) Tackett, B. S.; Clouthier, D. J. HPO does not follow Walsh's rules! Improved molecular structures from the spectroscopy of jet-cooled HPO and DPO. *J. Chem. Phys.* **2002**, *117*, 10604-10612.

(10) Ozeki, H.; Saito, S. Microwave spectra of HPO and DPO: molecular structure. *J. Mol. Spectrosc.* **2003**, *219*, 305-312.

(11) Grimminger, R.; Clouthier, D. J. The electronic spectrum of the previously unknown HAsO transient molecule. *J. Chem. Phys.* **2011**, *135*, 184308.

(12) Mok, D. K. W.; Lee, E. P. F.; Dyke, J. M. Simulation of the single-vibronic-level emission spectra of HAsO and DAsO. *J. Chem. Phys.* **2016**, *144*, 184303.

(13) Meyers, E. A.; Lipscomb, W. N. The crystal structure of hydroxylamine. *Acta Crystallogr.* **1955**, *8*, 583-587.

(14) Tsunekawa, S. Microwave Spectrum of Hydroxylamine. *J. Phys. Soc. Jpn.* **1972**, *33*, 167-174.

(15) Shi, K.-L.; Wang, R.-Q.; Mak, T. C. W. On the N-O bond length in free and *N*-protonated hydroxylamine, and redetermination of the crystal structure of hydroxylammonium chloride, $(H_3NOH)Cl$. *J. Mol. Struct.* **1987**, *160*, 109-116.

(16) Ahmad, I. K.; Ozeki, H.; Saito, S. Microwave spectroscopic detection of a transient phosphorus-bearing molecule, H_3PO. *J. Chem. Phys.* **1999**, *110*, 912-917.